

Laser-Splashed Three-Dimensional Plasmonic Nanovolcanoes for Steganography in Angular Anisotropy

Dejiao Hu,[†] Yudong Lu,[†] Yaoyu Cao,[†] Yanan Zhang,[†] Yi Xu,[‡] Wenxue Li,[§] Fuhua Gao,[§] Boyuan Cai,^{||} Bai-Ou Guan,[†] Cheng-Wei Qiu,^{*,†,‡,§} and Xiangping Li^{*,†}

[†]Guangdong Provincial Key Laboratory of Optical Fiber Sensing and Communications, Institute of Photonics Technology, and [‡]Department of Electronic Engineering, College of Information Science and Technology, Jinan University, Guangzhou 510632, China

[§]College of Physical Science and Technology, Sichuan University, Chengdu, Sichuan 610064, China

^{||}Nanophotonics Research Center, Shenzhen Key Laboratory of Microscale Optical Information Technology, and [#]SZU-NUS Collaborative Innovation Center for Optoelectronic Science and Technology, Shenzhen University, Shenzhen 518060, China

[⊥]Department of Electrical and Computer Engineering, National University of Singapore, 4 Engineering Drive 3, Singapore 117583

Supporting Information

ABSTRACT: Planar optics constructed from subwavelength artificial atoms have been suggested as a route to the physical realization of steganography with controlled intrinsic redundancy at single-pixel levels. Unfortunately, two-dimensional geometries with uniform flat profiles offer limited structural redundancy and make it difficult to create advanced crypto-information in multiplexed physical divisions. Here, we reveal that splashing three-dimensional (3D) plasmonic nanovolcanoes could allow for a steganographic strategy in angular anisotropy, with high resolution, full coloration, and transient control of structural profiles. Highly reproducible 3D morphologies of volcanic nanosplashes are demonstrated by creating a standardized recipe of laser parameters. Such single nanovolcanoes can be well controlled individually at different splashing stages and thus provide a lithography-free fashion to access various spectral responses of angularly coordinated transverse and vertical modes, leading to the full-range coloration. This chip-scale demonstration of steganographic color images in angular anisotropy unfolds a long-ignored scheme for structured metasurfaces and thereby provides a paradigm for information security and anticounterfeiting.

KEYWORDS: laser splashing, structural color, plasmonic nanostructures, angular anisotropy, steganography

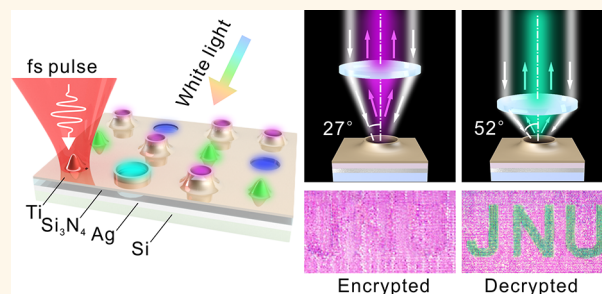


Image steganography hides secret information among other visible images,¹ holding great interest for information security and anticounterfeiting applications. Generally, its practice relies on a level of intrinsic redundancy of the constituent pixels forming an image where the redundant pixels can be altered to encrypt hidden information without the alternation being adversely perceptible.¹ On-chip realization of such steganographic strategies requires reducing the dimensionality of constituent pixels down to nanoscales. Although optical resonances of planar plasmonic nanostructures could be optimized to yield various functionalities of interest^{2–7} and have impelled substantial progress in flat optics such as metasurfaces,^{3,6,8–10} color prints at the optical diffraction limit^{4,9,11–18} and color filters,^{19–22} such as subwavelength nanostructures with uniform flat profiles (or limited stepwise heights), set up a fundamental limit for possible intrinsic

redundancy to encrypt hidden information in the physical properties such as polarizations^{12,21,23} and frequencies.^{16,24}

With broad applications widely featured (e.g., directional color routers,^{25,26} optical sensing,²⁰ and information encryption^{15,27,28}), the in-plane interferences between neighboring nanoantennas for unidirectional scattering²⁹ or between aperiodic plasmonic gratings for directional color sorters²⁰ are perceived as the “must have”, resulting in inevitably large footprints and unwanted cross-coupling. On-chip steganography based on single nanostructures exhibiting the desired intrinsic redundancy with full coloration and angle-sensitive

Received: May 26, 2018

Accepted: August 31, 2018

Published: August 31, 2018

responses remains an elusive goal. Nevertheless, this captivation is built upon the intrinsic knowledge in the absence of exquisite 3D profile control.

By introducing and manipulating a long-ignored degree of freedom (*i.e.*, vertical profiles of nano-objects), we report in this work an on-chip steganographic strategy in angular anisotropy by laser-printed three-dimensional (3D) plasmonic nanovolcanoes with various splashing morphologies. Single nanovolcanoes with varying subwavelength heights and volcanic profiles are printed by tightly focused femtosecond pulsed beams, in a highly deterministic way. The dexterity to control the 3D morphologies of single nanostructures allows angular encryption of different full-color images discernible at corresponding low and high incident angles, respectively. Our work may find applications in robust light control, color displays, multidimensional optical multiplexing, and anticounterfeiting.

RESULTS AND DISCUSSION

The concept of our angularly anisotropic steganography is illustrated in Figure 1. Single-layer architectures, consisting of

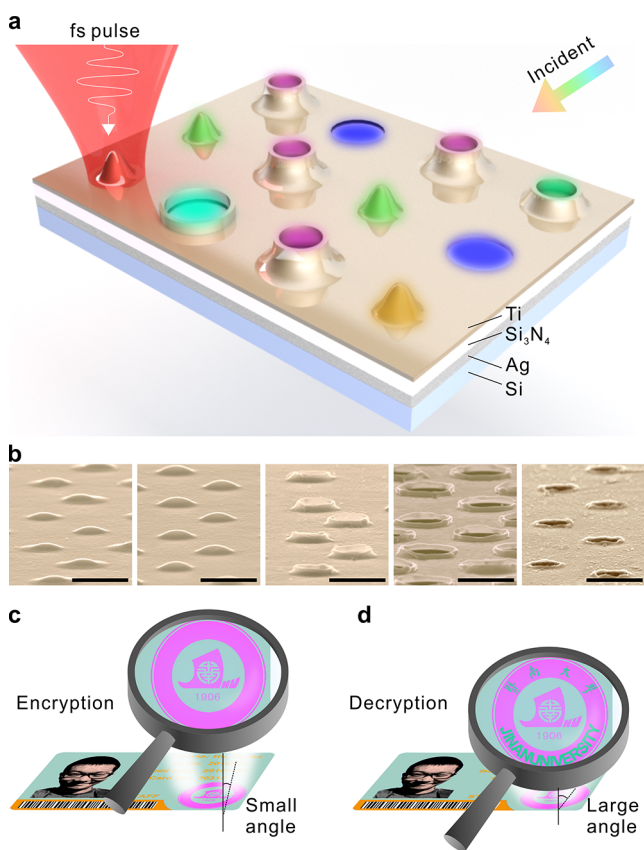


Figure 1. On-chip steganography in angular anisotropy by femtosecond pulse laser printed nanovolcanoes. (a) Schematic illustration of printed nanovolcanoes by a fs pulse and scattered color under oblique illuminations. The thicknesses of the silver, silicon nitride, and titanium layers are 80, 126, and 40 nm, respectively. (b) Scanning electron microscope image of nanovolcanoes with morphology evolution at different stages: bubbling crescents, cone-shaped, and well-like nanovolcanoes and nanocraters were obtained at fluences of ~ 135 , ~ 144 , ~ 180 , ~ 225 , and ~ 384 mJ/cm². Scale bars: 1 μ m. (c,d) Schematic illustration of on-chip image steganography encrypting and decrypting at small and large incident angles, respectively.

nanostructures resembling the splashing morphologies of volcanoes, are printed by a femtosecond (fs) pulsed laser.³⁰ Each of the individual plasmonic nanovolcanoes can exhibit a deterministic color and angle-sensitive spectral response, which are illustrated in Figure 1a. At a given illumination angle, the plasmonic nanovolcanoes can scatter colors ranging from blue to red depending on their morphologies. A metal–insulator–metal (MIM) configuration without any pre patterning is adopted to boost the splashing effects by quickly building up the localized fields. As titanium exhibits an absorption smaller than that of aluminum in the visible region,³¹ a thin titanium film of 40 nm thickness is chosen as the top metal layer to guarantee high color saturation. In addition, the formation of a thin (2–3 nm) oxide layer natively prevents the degradation and enhances the shelf life and durability of the printed plasmonic pixels.³² An 80 nm thick silver layer is chosen as the grounding because the silver film has the largest reflectance in the visible wavelength. A highly transparent layer of silicon nitride with a numerically optimized thickness of 126 nm is chosen as the spacer to facilitate the precise manipulation of the transient photothermal effects.

The MIM configuration forms a Fabry–Perot (FP) resonator and ensures a sufficient absorption of the incident pulse energy (Figure S1). Upon illumination of a single fs laser pulse (40 fs at 800 nm), the instantaneous energy goes sufficiently high enough to transiently heat the top titanium layer above its melting temperature, in the vicinity of the focal region. By exciting the FP mode with localized electric field confinement, the electromagnetic energy and hence the photothermal effect are dominantly concentrated in the top metal layer (Figure S2), allowing the fine control of the morphology and height of the printed nanovolcanoes through the translative or even ablative mass redistribution of the titanium thin film.^{33,34} Consequently, the printing of nanovolcanoes with variant morphologies and heights corresponding to different resonant frequencies or scattering colors becomes possible by precisely controlling the laser parameters in the focal profiles and pulse fluences (Figure 1b). A full library of nanovolcanoes by the continuous tuning of scattering colors across the entire visible spectrum is obtained with different laser parameters (Figure S3). Such subwavelength-scale nanostructures with different volcanic morphologies and heights can support angularly coordinated transverse and vertical modes at different resonances, allowing angularly anisotropic color appearances for encrypting hidden color images at different incident angles under white light illumination. Consequently, a school badge made of corresponding nanovolcanoes could contain embedded encrypted information only discernible at the prefixed decoding angle (Figure 1d,e).

By precisely modulating the laser energy density, the sophisticated profile of volcano-shaped nanostructures can be continuously tuned in a controllable means. Depending on the single-pulse irradiation, the redistribution of the molten titanium thin film can evolve from a bubbling crescent to cone-shaped to well-like nanovolcanoes. Further increased laser dose will lead to a rapid ablation, forming size-controllable nanocraters. Figure 2a,b shows the scanning electron microscopy (SEM) images of printed nanovolcanoes with representative morphologies. Interestingly, scattering colors from the blue, green, and red tones (indicating a full-color generation) can be achieved, as shown in Figure 2c and the corresponding insets. The simulated spectra based on the

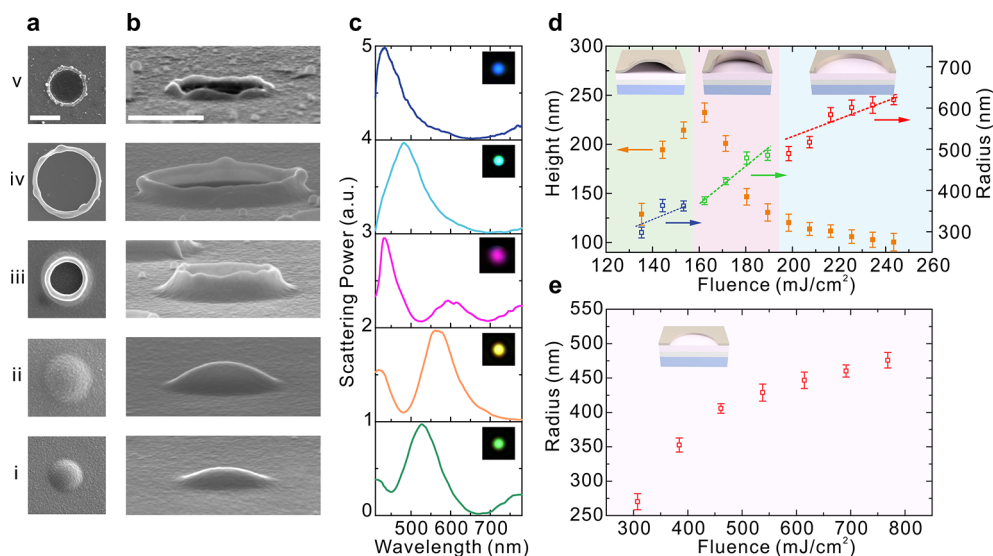


Figure 2. Splashing morphologies of nanovolcanoes and scattering spectra. (a,b) Top and side view SEM images of nanovolcanoes at different splashing stages (bubbling crescents (i,ii), cone-shaped (iii), and well-like (iv) nanovolcanoes, and nanocraters (v)). Scale bars: 500 nm. (c) Experimental scattering spectra from the nanovolcanoes shown in (a,b). The experimental spectra are acquired from single nanostructures in a home-built dark-field microscope employing a supercontinuum laser source as the illumination. The incident angle is set at approximately 27° through an objective lens with a large back aperture (UPlanSApo, $20\times/0.75$, Olympus Co.). The insets show the scattering images of single nanostructures taken when measuring the spectra. (d) Morphology evolution of the nanovolcanoes as a function of energy fluences (NA = 0.4), revealing three regions of splashing morphologies. (e) Evolution of the radius of the nanocraters against the energy fluence fabricated with an objective lens of NA = 0.75. For small fluences, the generated nanostructures have no distinct scattering features in the visible region. Consequently, only nanostructures produced by fluences larger than 307 mJ/cm^2 are investigated.

measured 3D profiles are presented in Figure S4, exhibiting good congruence with the experimental observation of morphology-dependent scattering.

Even though the formation of splashing morphologies is generally perceived as a non-equilibrium process, the dynamics can be further elucidated in a simplified two-stage physical model based on analytical two-temperature (2T) calculations^{5,33,35} and a nanoscale hydrodynamic motion.^{33,34} This model is built upon recent theoretical developments separating slow and fast physical processes (see the supporting discussions). The transient absorbed electromagnetic energy density can be expressed as³⁶

$$q(x, y, z, t) = \frac{\omega}{2} \varepsilon''(\omega, x, y, z) \varepsilon_0 |E(\omega, x, y, z, t)|^2 \quad (1)$$

where ω is the center frequency, ε'' is the imaginary part of the relative permittivity, ε_0 is the permittivity of vacuum, and $|E(\omega, x, y, z, t)|$ is the envelope of the Gaussian-shaped time-varying electric field. The absorbed electromagnetic energy can be converted into a concentrated and transient heat effect through a 2T relaxation procedure and dissipates quickly into the continuous titanium thin film. Initially, the heating of electrons and subsequent thermalization of the lattices by an intense electron–lattice interaction normally takes place within the first few picoseconds (Figure S2). The heating effect is dominantly concentrated in the vicinity of the focal spot with a size of $1.2\ \mu\text{m}$, considering an objective with a numerical aperture (NA) of 0.4.

The separation of the molten film from the substrate starts as a consequence of expansion waves generated by the isochoric laser heating of the metal film.^{33,34} The separation velocity can be estimated by³³

$$v \sim \frac{Z_f}{Z_s} \times \frac{p(r)}{(Z_f + Z_s)} \quad (2)$$

where $p(r)$ is the time-average pressure within the titanium film over the sonic time scale (supporting discussion), r is the radius to the center of the focal spot, and Z_s and Z_f are acoustic impedances of the underneath layer and the titanium film, respectively. The vertical separation velocity is maximized at the center and approaches zero at the edge of the irradiated region. After a separation velocity was acquired, the molten film starts to fly outward. Next, the surface tension slows down the moving titanium film. The heat dissipation to the surroundings happens simultaneously and is responsible for immobilizing the morphologies of the splashing films, giving rise to the formation of nanovolcanoes with controlled geometries and heights.

Figure 2d shows the evolution of the nanovolcanoes as a function of energy fluences given by an objective lens with NA = 0.4. It is revealed that there are three major stages of morphology engineering. At low energies (fluence of ~ 135 to 157 mJ/cm^2), the rapid dissipation of heat leads to a quick recrystallization of the molten titanium film, resulting in the formation of bubbling crescents. If the pulse energy exceeds a fluence threshold of $\sim 157\text{ mJ/cm}^2$, then the center of the irradiated film acquires a considerably large velocity. In contrast, the outer area separates from the substrate in a slow manner and undergoes a quick recrystallization due to heat transfer to the surrounding titanium film. This mismatch results in the rupture of the central zone from the film, forming cone-shaped nanovolcanoes. If the deposited energy is even higher, then a well-like volcanic morphology is formed due to the residual heat on the nanovolcano that softens the wall and makes it lower, thicker, and smoother. From the height and radius of the nanostructures, it can be seen that the height

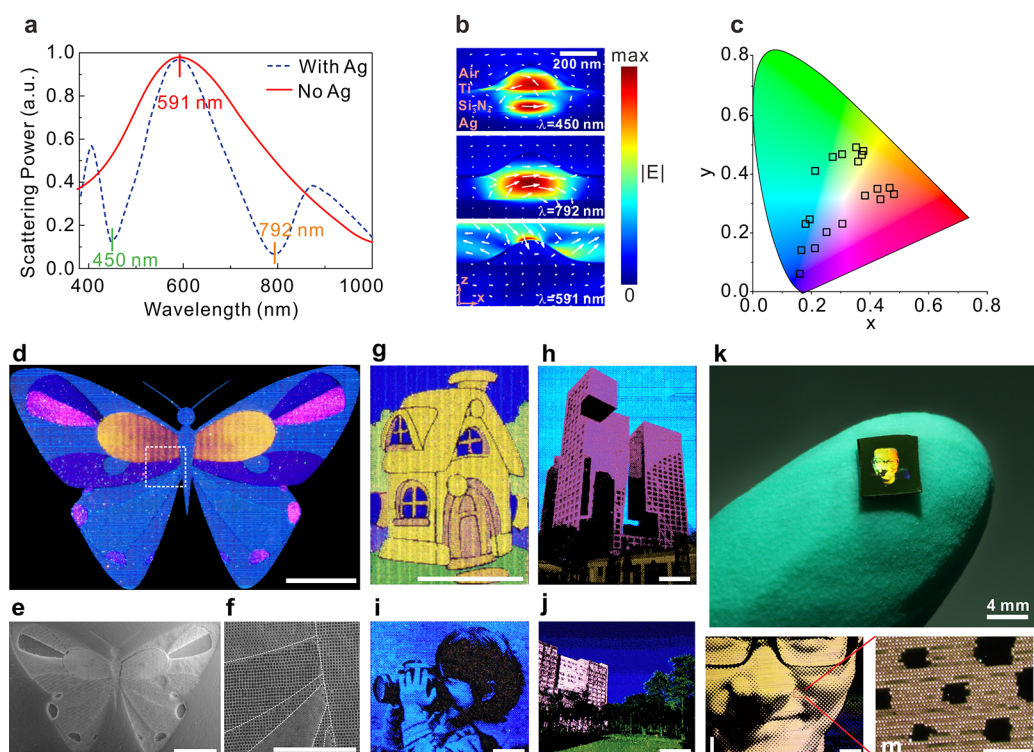


Figure 3. Enhanced color saturation and up-scalable lithography-free printing. (a) Simulated scattering power from a bubbling crescent (with a height of 122 nm and diameter of 600 nm) with and without a grounding silver layer. The Fano-like resonance-induced asymmetric line shape and spectral narrowing effect are clearly revealed. (b) Electric field distribution in the $y = 0$ plane for the three wavelengths marked in (a), where the white arrows represent the displacement current flows. The modes at $\lambda = 450$ nm and $\lambda = 792$ nm are the second and first order of FP resonances, respectively, resembling the narrow band subradiant modes (top and middle rows, with Ag), whereas the plasmonic resonance at $\lambda = 591$ nm offers the wide band super-radiant mode (bottom row, without Ag). (c) Chromaticity coordinates (CIE1931 color space) of the achieved colors (black boxes), indicating a large range. (d–m) Collection of images printed by fs laser beams in continuous tone (d–g) and half-tone modes (h–m), showing the capability of high-resolution printing with high color fidelity. Scale bars: 200 μm (d,e,g–j,l), 50 μm (f), and 20 μm (m).

increases along the pulse energy and reaches the maximum in the cone-shaped volcanic section, and then, it decreases and approaches approximately 100 nm, such as in the well-like regime. For even larger deposition fluence obtained with an objective lens of NA = 0.75, the titanium film is quickly ablated, forming nanocraters, whose radius increases with the energy fluence (Figure 2e). The fine control of the morphologies and heights of such nanovolcanoes can thus be accomplished reliably by the focal profile and laser energy density.

It is found that the top plasmonic volcanic nanostructures can support current-driven vertical modes along the axis of symmetry of the nanovolcano and transverse modes, with charges oscillating upon the curvature of the metal rim resonant at different frequencies, similar to plasmonic nanoparticles with a reduced symmetry^{37,38} (Figure S5). As mentioned before, the MIM configuration supports FP resonant modes depending on the thickness of the spacer (Figure S6), coupled with the plasmonic resonances of the nanovolcanoes atop it. Ultimately, this coupling results in complex current-driven modes which are responsible for the full-range visible light scattering in the printed architecture, as illustrated in Figure 2.

It is noteworthy that such coupling can further lead to a Fano-like^{39–41} asymmetric scattering spectrum once their fields can form a destructive interference in the far-field (Figure 3a,b). This Fano-like line shape can significantly

narrow the plasmonic resonances, resulting in a color palette with enhanced saturation. Figure 3d shows the chromaticity coordinates of achievable colors, calculated based on the scattering spectra. It reveals that primary colors used in traditional printing from blue, green, and red can all be achieved. By synergistically moving the laser focus (Figure S7),³⁰ monochrome and color images scaling from hundreds of micrometers to several millimeters can be demonstrated with a high fidelity (Figure 3d–m and Figure S8).

The high spatial resolution of the pixel is one of the most notable advantages of laser printing. Figure 3d illustrates a color butterfly 1 mm wide with a resolution of 12 700 dpi (pixel-to-pixel distance of 2 μm) printed at different laser parameters. The SEM image of the whole sample and the selected region within the white dashed box in Figure 3d are shown in Figure 3e,f, respectively. High-resolution chip-scale printings up to 20 000 dpi can also be achieved using the facile laser printing (Figure S8). To show the capability of up-scalable printing, a subcentimeter portrait was printed with a high resolution and high fidelity (Figure 3k–m and Figure S9).

The nanovolcanic structure alone can support both p-polarization vertical modes stemming from electroinductive plasmonic responses and polarization-insensitive transverse modes due to the rotational symmetry. Consequently, a prominent angular mode coordination effect from transverse-mode-dominant to vertical-mode-dominant can be achieved when increasing the incident angles of p-polarized illumination

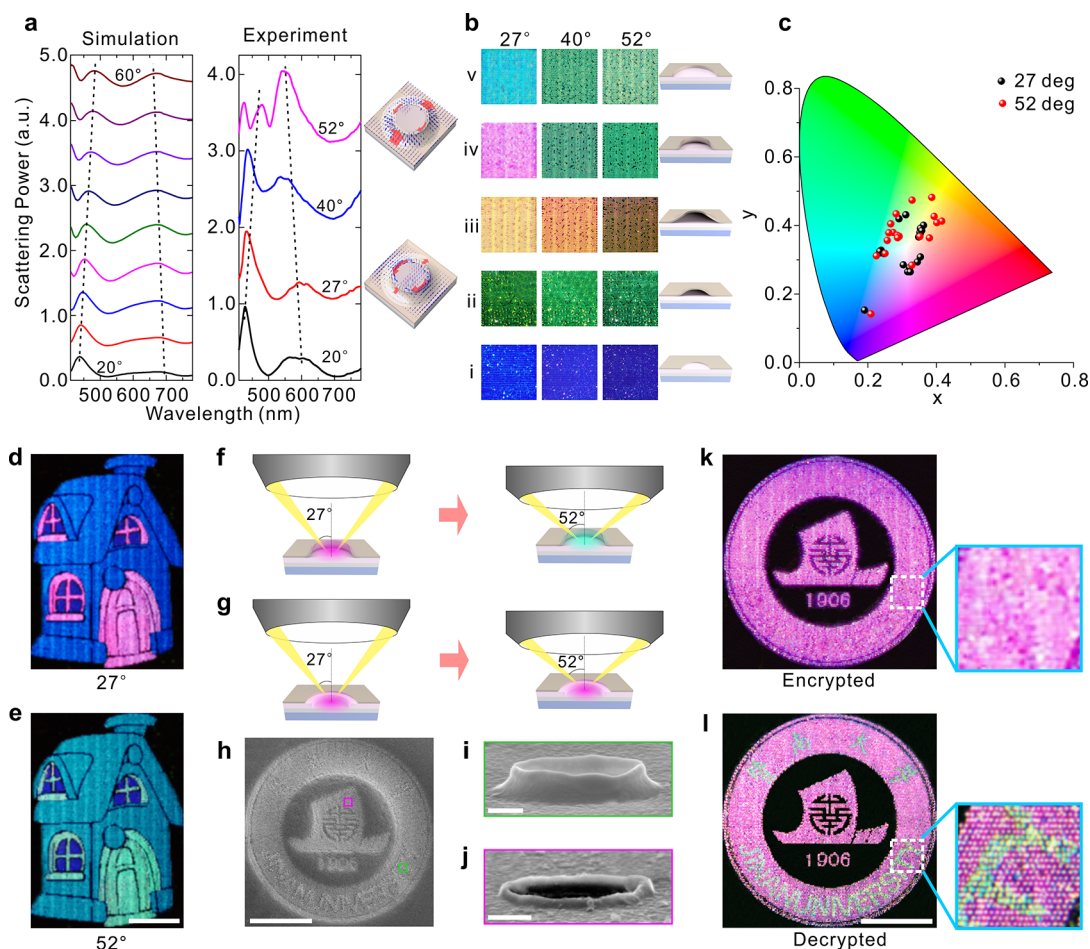


Figure 4. Angularly anisotropic color appearance and on-chip image steganography. (a) Simulated and experimental scattering spectral variation as a function of the incident angle from a single nanovolcano. The dashed lines are a guide for the eyes. The insets illustrate the dominant modes corresponding to the longer wavelength scattering peak at illumination angles of 27 and 52°, respectively, revealing that the transverse current-driven modes are dominant at low incident angles and the vertical current-driven modes are dominant at large incident angles. The red arrows represent the displacement currents supported in the nanovolcano. (b) Angularly anisotropic color appearances of the five representative nanovolcanoes in Figure 2 as a function of the incident angle. (c) CIE1931 chromaticity coordinates of colors from the library nanostructures under incident angles of approximately 27 and 52°. (d,e) Cartoon image that changes color appearances viewed at low and high incident angles. (f,g) Sketch of the color variation of the nanovolcano and nanocrater under dark-field objective lenses with different incident angles. (h–j) SEM images of a school badge composed of these two kinds of printed nanostructures: the cone-shaped nanovolcano (g) and the nanocrater (h). (k,l) Image steganography in angular anisotropy achieved depending on the variation of color appearances in (f,g). Logo used with permission from Jinan University. The images are viewed under incident angles of approximately 27° (MPlanFL N, 5 \times /0.15 BD, Olympus Co.) and 52° (MPlanFL N, 20 \times /0.45 BD, Olympus Co.). Scale bars: 100 μ m (e,h,l) and 200 nm (i,j).

(Figure S10). In addition, such mode competition can also introduce a shift in the relative phase to modify the interference of the Fano-like spectrum,^{39–41} as illustrated in simulated and measured spectral variation from single cone-shaped nanovolcanoes (Figure 4a). The inset clearly reveals that vertical current-driven modes dominate at the large oblique angle, whereas the transverse current-driven modes are more pronounced at the low incident angle. The experimental results qualitatively agree with the simulation. The discrepancy in the peak resonant wavelength could be attributed to the geometrical imperfection of laser fabrication.

Figure 4b depicts the evolution of the color palettes from these five representative nanovolcanoes as a function of the incident angle. It can be seen that scattering colors from these low-profile nanostructures exhibit little or even negligible variations when the incident angle increases from 27 to 52° (Figure 4b, rows i and ii). However, for bubbling crescents with sufficient height to support the enlarged amplitudes of

vertical modes, a color change from yellow to orange and dark orange is observed (Figure 4b, row iii). Figure 4b row iv showcases a prominent case of color variation occurring on a cone-shaped nanovolcano with a height of 230 nm. When this sample is illuminated with white light at incident angles from 27 to 52°, the scattering color metamorphoses drastically from pink to cyan-green. A full library of the angle-anisotropic colors in these nanostructures with varying volcanic profiles and heights are given in Figure S10. The angular color tunability can be directly visualized in the CIE1931 chromaticity coordinates of the scattering colors at incident angles of 27 and 52° simulated in Figure 4c. Figure 4d,e presents a color print with angularly anisotropic appearances, viewed at low and large incident angles.

The angle-steerable coloration of such nanovolcanoes offers a route to image steganography in angular anisotropy. As a proof of concept, a chip-scale badge of “Jinan University” was printed with position-dependent laser energy doses exhibiting

angle-insensitive and drastic angle-tunable colors, as shown in the SEM images in Figure 4h–j. At a small incident angle of 27°, the encrypted characters are hidden in the pink background (Figure 4k). At the incident angle of 52°, the encrypted characters displaying a cyan-green color clearly arise from the pink background (Figure 4l). Comprehensive angularly multiplexed color printing is further explored with four categories of pixels, and a bee and a flower can be distinctly viewed at 27 and 52°, respectively (Figure S11).

CONCLUSIONS

In conclusion, we have presented fs laser-printed nanovolcanoes exploiting subwavelength and 3D morphologies, which allow the experimental demonstration of on-chip steganography from angular anisotropy. The proposed method is implemented by precisely controlling the transient local heat and subsequent translative mass redistributions of molten metal films by the pulsed laser interaction with MIM configurations. The method avoids the nanofabrication technologies that are usually resorted to in such cases, such as e-beam lithography or nanoimprinting. Such a laser printing technique can thus be ready for the scalable production of imprints on the order of millimeters and even larger areas. It can dramatically push the state-of-the-art and enrich the emerging knowledge base of plasmonic color generation.^{4,11,13,14} Furthermore, the coordination between vertical and transverse modes of the nanovolcanoes induces an angle-anisotropic spectral response (also known as color generation) and enables angularly anisotropic image steganography. It provides a viable recording scheme for multidimensional optical multiplexing with additional physical properties,¹² information encryption,^{15,16,23,24} and anticounterfeiting^{27,28} with ultrasecurity.

METHODS

Sample Preparation. The multilayers were prepared using a heat/electron beam evaporator at a working pressure of about $\sim 2 \times 10^{-4}$ Pa. An 80 nm thick layer of silver was deposited onto the silicon substrate using heat evaporation at a rate of 2.97 \AA s^{-1} . Next, a 126 nm thick layer of silicon nitride was deposited onto the silver layer using electron beam evaporation at a rate of 1.3 \AA s^{-1} . Finally, a 40 nm thick titanium layer was coated onto the silicon nitride layer using electron beam evaporation at a rate of 1.7 \AA s^{-1} . During the evaporation process, the sample chamber was kept at a constant temperature of 30 °C, and the sample holder was rotated at 40 rpm to maintain uniform deposition.

Laser Printing. The sample was mounted to a 3D translation stage that was controlled by the computer (Figure S7). The 40 fs laser pulse was attenuated and focused onto the sample by an objective lens. The attenuator was used to tune the pulse energy to the required values. A camera was used to collect the image reflected back from the sample surface. The desired image was printed by synergistic movement between the focal spot and the 3D stage.

Sample Characterization and Optical Measurements. Dark-field optical images and scattering spectra of the color pixels were obtained to investigate the optical responses of the fabricated structures. Optical images were captured using a conventional upright dark-field scattering microscope (Olympus, BX53, Olympus Co.). Images of the samples were acquired by a dark-field objective lens. An objective lens of low NA (MPlanFL N, 5 \times /0.15 BD, Olympus Co.) provided an incident angle of approximately 27°, and another two objective lenses of high NA (MPlanFL N, 10 \times /0.3 BD, Olympus Co. and MPlanFL N, 20 \times /0.45 BD, Olympus Co.) yielded incident angles of approximately 40 and 52°, respectively. The scattering spectra from a single nanostructure were measured by a home-built dark-field microscope, where a supercontinuum laser source (SC-PRO, YSL

Photonics Co.) was used as the illumination and a fiber spectrometer (USB4000, Ocean Optics Co.) was employed to acquire the scattering spectrum (Figure S12).

Numerical Simulations. The optical response of the color pixels were modeled using FDTD (Lumerical FDTD Solutions). The complex refractive indices of silicon, silver, and titanium were taken from Palik,³¹ and the index of silicon nitride was set as 2.05. A total-field/scattered-field source was illuminated onto the nanostructure from the left side at an oblique angle. Perfectly matched layer boundary conditions were defined around the nanostructure at a minimal of half a wavelength away. Then, the scattering power collected by the objective lens was calculated by evaluating the near-to far-field projection over a cone defined by the NA of the objective lens.

ASSOCIATED CONTENT

Supporting Information

The Supporting Information is available free of charge on the ACS Publications website at DOI: 10.1021/acsnano.8b03964.

Photothermal and nanoscale hydrodynamics process, mode analysis, fabrication and measurement of optical setup, high-resolution and scalable prints, and color difference analysis (PDF)

AUTHOR INFORMATION

Corresponding Authors

*E-mail: chengwei.qiu@nus.edu.sg.

*E-mail: xiangpingli@jnu.edu.cn.

ORCID

Dejiao Hu: 0000-0003-2491-909X

Yaoyu Cao: 0000-0003-1530-2346

Cheng-Wei Qiu: 0000-0002-6605-500X

Xiangping Li: 0000-0003-0955-2613

Notes

The authors declare no competing financial interest.

ACKNOWLEDGMENTS

This research was supported by National Key R&D Program of China (YS2018YFB110012), National Natural Science Foundation of China (NSFC) (Grant Nos. 21317137, 61522504, and 91750110), and Guangdong Provincial Innovation and Entrepreneurship Project (Grant No. 2016ZT06D081). C.-W.Q. acknowledges the financial support from the National Research Foundation, Prime Minister's Office, Singapore under its Competitive Research Program (CRP award NRF-CRP15-2015-03). The authors thank Professor Yaohua Mai (Jinan University) for access to the SEM facilities.

REFERENCES

- (1) Morkel, T.; Eloff, J. H.; Olivier, M. S. *An Overview of Image Steganography*; ISSA, 2005; pp 1–11.
- (2) Kosako, T.; Kadoya, Y.; Hofmann, H. F. Directional Control of Light by a Nano-Optical Yagi-Uda Antenna. *Nat. Photonics* **2010**, *4*, 312–315.
- (3) Yu, N.; Genevet, P.; Kats, M. A.; Aieta, F.; Tietienne, J.-P.; Capasso, F.; Gaburro, Z. Light Propagation with Phase Discontinuities: Generalized Laws of Reflection and Refraction. *Science* **2011**, *334*, 333–337.
- (4) Kumar, K.; Duan, H.; Hegde, R. S.; Koh, S. C. W.; Wei, J. N.; Yang, J. K. W. Printing Colour at the Optical Diffraction Limit. *Nat. Nanotechnol.* **2012**, *7*, 557–561.
- (5) Li, X.; Lan, T.-H.; Tien, C.-H.; Gu, M. Three-Dimensional Orientation-Unlimited Polarization Encryption by a Single Optically Configured Vectorial Beam. *Nat. Commun.* **2012**, *3*, 998.

- (6) Ren, H.; Li, X.; Zhang, Q.; Gu, M. On-Chip Noninterference Angular Momentum Multiplexing of Broadband Light. *Science* **2016**, *352*, 805–809.
- (7) Deng, Z.-L.; Deng, J.; Zhuang, X.; Wang, S.; Li, K.; Wang, Y.; Chi, Y.; Ye, X.; Xu, J.; Wang, G. P.; et al. Diatomic Metasurface for Vectorial Holography. *Nano Lett.* **2018**, *18*, 2885–2892.
- (8) Ni, X.; Kildishev, A. V.; Shalae, V. M. Metasurface Holograms for Visible Light. *Nat. Commun.* **2013**, *4*, 2807.
- (9) Clausen, J. S.; Højlund-Nielsen, E.; Christiansen, A. B.; Yazdi, S.; Grajower, M.; Taha, H.; Levy, U.; Kristensen, A.; Mortensen, N. A. Plasmonic Metasurfaces for Coloration of Plastic Consumer Products. *Nano Lett.* **2014**, *14*, 4499–4504.
- (10) Yu, N.; Capasso, F. Flat Optics with Designer Metasurfaces. *Nat. Mater.* **2014**, *13*, 139–150.
- (11) Kristensen, A.; Yang, J. K.; Bozhevolnyi, S. I.; Link, S.; Nordlander, P.; Halas, N. J.; Mortensen, N. A. Plasmonic Colour Generation. *Nat. Rev. Mater.* **2017**, *2*, 16088.
- (12) Goh, X. M.; Zheng, Y.; Tan, S. J.; Zhang, L.; Kumar, K.; Qiu, C.-W.; Yang, J. K. W. Three-Dimensional Plasmonic Stereoscopic Prints in Full Colour. *Nat. Commun.* **2014**, *5*, 5361.
- (13) Gu, Y.; Zhang, L.; Yang, J. K.; Yeo, S. P.; Qiu, C.-W. Color Generation Via Subwavelength Plasmonic Nanostructures. *Nanoscale* **2015**, *7*, 6409–6419.
- (14) Zhu, X.; Vannahme, C.; Højlund-Nielsen, E.; Mortensen, N. A.; Kristensen, A. Plasmonic Colour Laser Printing. *Nat. Nanotechnol.* **2016**, *11*, 325–329.
- (15) Xue, J.; Zhou, Z.-K.; Wei, Z.; Su, R.; Lai, J.; Li, J.; Li, C.; Zhang, T.; Wang, X.-H. Scalable, Full-Colour and Controllable Chromotropic Plasmonic Printing. *Nat. Commun.* **2015**, *6*, 8906.
- (16) Duan, X.; Kamin, S.; Liu, N. Dynamic Plasmonic Colour Display. *Nat. Commun.* **2017**, *8*, 14606.
- (17) Guay, J.-M.; Calà Lesina, A.; Côté, G.; Charron, M.; Poitras, D.; Ramunno, L.; Berini, P.; Weck, A. Laser-Induced Plasmonic Colours on Metals. *Nat. Commun.* **2017**, *8*, 16095.
- (18) Clark, A. W.; Cooper, J. M. Plasmon Shaping by Using Protein Nanoarrays and Molecular Lithography to Engineer Structural Color. *Angew. Chem., Int. Ed.* **2012**, *51*, 3562–3566.
- (19) Xu, T.; Wu, Y.-K.; Luo, X.; Guo, L. J. Plasmonic Nanoresonators for High-Resolution Colour Filtering and Spectral Imaging. *Nat. Commun.* **2010**, *1*, 1058.
- (20) Davis, M. S.; Zhu, W.; Xu, T.; Lee, J. K.; Lezec, H. J.; Agrawal, A. Aperiodic Nanoplasmonic Devices for Directional Colour Filtering and Sensing. *Nat. Commun.* **2017**, *8*, 1347.
- (21) Li, Z.; Clark, A. W.; Cooper, J. M. Dual Color Plasmonic Pixels Create a Polarization Controlled Nano Color Palette. *ACS Nano* **2016**, *10*, 492–498.
- (22) Heydari, E.; Sperling, J. R.; Neale, S. L.; Clark, A. W. Plasmonic Color Filters as Dual-State Nanopixels for High-Density Microimage Encoding. *Adv. Funct. Mater.* **2017**, *27*, 1701866.
- (23) Yue, F.; Zhang, C.; Zang, X.-F.; Wen, D.; Gerardot, B. D.; Zhang, S.; Chen, X. High-Resolution Grayscale Image Hidden in a Laser Beam. *Light: Sci. Appl.* **2017**, *7*, 17129.
- (24) Walter, F.; Li, G.; Meier, C.; Zhang, S.; Zentgraf, T. Ultrathin Nonlinear Metasurface for Optical Image Encoding. *Nano Lett.* **2017**, *17*, 3171–3175.
- (25) Shegai, T.; Chen, S.; Miljković, V. D.; Zengin, G.; Johansson, P.; Käll, M. A Bimetallic Nanoantenna for Directional Colour Routing. *Nat. Commun.* **2011**, *2*, 481.
- (26) Coenen, T.; Bernal Arango, F.; Femius Koenderink, A.; Polman, A. Directional Emission from a Single Plasmonic Scatterer. *Nat. Commun.* **2014**, *5*, 3250.
- (27) Sauvage-Vincent, J.; Tonchev, S.; Veillas, C.; Reynaud, S.; Jourlin, Y. Optical Security Device for Document Protection Using Plasmon Resonant Transmission through a Thin Corrugated Metallic Film Embedded in a Plastic Foil. *J. Eur. Opt. Soc.-Rapid* **2013**, *8*, 13015.
- (28) Lochbihler, H. Polarizing and Angle-Sensitive Color Filter in Transmittance for Security Feature Applications. *Adv. Opt. Technol.* **2015**, *4*, 71–77.
- (29) Curto, A. G.; Volpe, G.; Taminiau, T. H.; Kreuzer, M. P.; Quidant, R.; van Hulst, N. F. Unidirectional Emission of a Quantum Dot Coupled to a Nanoantenna. *Science* **2010**, *329*, 930–933.
- (30) Li, X.; Ren, H.; Chen, X.; Liu, J.; Li, Q.; Li, C.; Xue, G.; Jia, J.; Cao, L.; Sahu, A.; et al. Athermally Photoreduced Graphene Oxides for Three-Dimensional Holographic Images. *Nat. Commun.* **2015**, *6*, 6984.
- (31) Palik, E. D. *Handbook of Optical Constants of Solids*; Academic Press, 1998.
- (32) Lütjering, G.; Williams, J. C. *Titanium*; Springer, 2007.
- (33) Inogamov, N.; Zhakhovskii, V.; Khokhlov, V. Jet Formation in Spallation of Metal Film from Substrate under Action of Femtosecond Laser Pulse. *J. Exp. Theor. Phys.* **2015**, *120*, 15–48.
- (34) Wang, X. W.; Kuchmizhak, A. A.; Li, X.; Juodkazis, S.; Vitrik, O. B.; Kulchin, Y. N.; Zhakhovsky, V. V.; Danilov, P. A.; Ionin, A. A.; Kudryashov, S. I.; Rudenko, A. A.; Inogamov, N. A. Laser-Induced Translative Hydrodynamic Mass Snapshots: Noninvasive Characterization and Predictive Modeling Via Mapping at Nanoscale. *Phys. Rev. Appl.* **2017**, *8*, 044016.
- (35) Nolte, S.; Momma, C.; Jacobs, H.; Tünnermann, A.; Chichkov, B. N.; Wellegehausen, B.; Welling, H. Ablation of Metals by Ultrashort Laser Pulses. *J. Opt. Soc. Am. B* **1997**, *14*, 2716–2722.
- (36) Baffou, G.; Quidant, R. Thermo-Plasmonics: Using Metallic Nanostructures as Nano-Sources of Heat. *Laser Photonics Rev.* **2013**, *7*, 171–187.
- (37) Mirin, N. A.; Halas, N. J. Light-Bending Nanoparticles. *Nano Lett.* **2009**, *9*, 1255–1259.
- (38) King, N. S.; Li, Y.; Ayala-Orozco, C.; Brannan, T.; Nordlander, P.; Halas, N. J. Angle- and Spectral-Dependent Light Scattering from Plasmonic Nanocups. *ACS Nano* **2011**, *5*, 7254–7262.
- (39) Luk'yanchuk, B.; Zheludev, N. I.; Maier, S. A.; Halas, N. J.; Nordlander, P.; Giessen, H.; Chong, C. T. The Fano Resonance in Plasmonic Nanostructures and Metamaterials. *Nat. Mater.* **2010**, *9*, 707–715.
- (40) Miroshnichenko, A. E.; Flach, S.; Kivshar, Y. S. Fano Resonances in Nanoscale Structures. *Rev. Mod. Phys.* **2010**, *82*, 2257–2298.
- (41) Fan, P.; Yu, Z.; Fan, S.; Brongersma, M. L. Optical Fano Resonance of an Individual Semiconductor Nanostructure. *Nat. Mater.* **2014**, *13*, 471–475.